Dynamic full-field imaging of rupture radiation: Material contrast governs source mechanism

Aichele J.[1,2*], Latour S.[3], Catheline S.[1], and Roux P.[2]

[1]Laboratory of Therapeutic Applications of Ultrasound, INSERM & University of Lyon, Lyon, France
[2]ISTerre, Univ. Grenoble Alpes, Univ. Savoie Mont Blanc, CNRS, IRD, Univ. Gustave Eiffel, Grenoble, France
[3]Institute of Astrophysics and Planetology, IRAP & University of Toulouse III, Toulouse, France

*currently at Department of Earth Sciences, Institute of Geophysics, Swiss Federal Institute of Technology, Zürich, Switzerland

Corresponding author: Aichele J., `johannes.aichele@rwth-aachen.de`

Abstract

In seismology, the rupture mechanism of an earthquake, a glacier stick-slip and a landslide is not directly observed, but inferred from surface measurements. In contrast, laboratory experiments can illuminate near field effects, which reflect the rupture mechanism but are highly attenuated in the case of real-world surface data. We directly image the elastic wave-field of a nucleating rupture non-invasively in its near-field with ultrasound speckle correlation. Our imaging yields the particle velocity of the full shear wave field at the source location and inside the 3D frictional body. We experimentally show that a strong bimaterial contrast, as encountered in environmental seismology, yields a unidirectional or linear force mechanism for pre-rupture microslips and decelerating supershear ruptures. A weak contrast, characteristic for earthquakes, generates a double-couple source mechanism for sub-Rayleigh ruptures, sometimes preceded by slow deformation at the interface. This deformation is reproduced by the near field of a unidirectional force.

Key Points:

- Noninvasive elastic near-field laboratory observations reveal source mechanisms of micro-slips, supershear and sub-Rayleigh ruptures.
- Strong material contrasts as encountered in glacier stick-slip and landslides cause single force micro-slips and supershear ruptures.
- Weak material contrasts lead to a double-couple mechanism, sometimes preceded by the near field radiation of a slowly rising single force.

Plain Language Summary

Earthquakes, avalanches, icequakes and landslides originate from a common process: rupture at a material interface. During a rupture, for example when a landslide slips, a characteristic pattern of seismic waves is created. This pattern differs at the earth's surface and the rupture interface, which is the source of the seismic waves inside the earth. Usually scientists only measure the waves arriving at the surface and need to deduce the wave pattern inside the earth from the surface measurement. We build a laboratory experiment which enables us to film wave propagation around the rupture surface, as if we had a camera inside the material. We film waves emitted during and prior to a rupture. For a soft material on a hard surface, such as encountered in icequakes or landslides, a single force model better explains the observed wave pattern than the commonly used model of four distributed forces. The rupture moves faster than shear waves propagate which results in a supershear cone, the elastic equivalent to the acoustic Mach cone created by supersonic aircrafts. For two materials of similar hardness, such as encountered in earthquakes, the classic model of four forces better explains the ruptures, which travel at sub-shear speed.

1 Introduction

For most earthquakes, the longstanding discussion on the appropriate force representation of the earthquake source has been decided in favor of the double-couple (DC) source. It is the body force equivalent to slip on a fault and consists of two force couples acting at the earthquake source point (Pujol, 2003; Aki & Richards, 2009). However, other rupture observations such as icequakes, landslides, induced seismicity and deep earthquakes are not always well reproduced by a standard double-couple model. For example, Ben-Zion and Ampuero (2009) theoretically show that brittle rupture is associated with a non-double-couple damage related source term. Kwiatek et al. (2011); Kwiatek and Ben-Zion (2013) discuss the presence of tensile opening during induced seismicity and aftershocks of a Mw

1.9 earthquake. In the case of glacial sliding, Ekström et al. (2003) report that a single force centroïd inversion shows a better match than standard moment tensor inversion (Harvard-CMT). In the laboratory, Lykotrafitis and Rosakis (2006) found indications for wrinkle-like rupture and tensile opening in a Homalite-on-steel friction experiment.

Inversion for earthquake sources is mostly done in the far-field and suffers from ambiguity. With the exception of volcanic seismicity, where hypocenters are shallow (Lokmer & Bean, 2010), the seismic near field suffers strong attenuation and is often concealed by ambient noise. In contrast to real-world seismic data, laboratory rupture experiments allow for dense instrumentation and direct imaging of rupture propagation. For example, the first unambiguous proof of supershear rupture was provided by strain imaging through photo-elastic experiments of sliding Homalite plates by Rosakis and Coker (1999). Recently, the group retrieved wave motion displacements of supershear ruptures through digital image correlation (Rubino et al., 2020, 2022). Latour et al. (2011, 2013) introduced a new direct rupture imaging method using ultrafast ultrasound imaging that allows for observation of shear wave radiation during rupture propagation in soft materials: the particle velocity of a propagating shear wave is retrieved through speckle tracking of subsequent ultrasound (US) backscatter images. In contrast to photo-elasticity, this method is not restricted to 2D setups. Their results show that during hydrogel-on-sandpaper friction the depinning of the gel from the sandpaper is well matched by a singular bell shaped (Gaussian) shear point force. They also directly observed the effects of barriers on rupture propagation on a hydrogel-glass interface with a granular inter-layer. At first glance hydrogels might seem counterintuitive as a material choice in rupture experiments. However, they have been extensively used as geological analogues (van Otterloo & Cruden, 2016). An historic example is the jelly experiment of Reid (1910) that led to the elastic rebound theory. More recent examples include a subduction-analogue gelatin setup (Corbi et al., 2011),(Corbi et al., 2017) and volcanic modeling (Kavanagh et al., 2018).

Here we investigate the source mechanism of the failure of a granular asperity in a laboratory friction experiment using a new setup based on the methodology introduced by Latour et al. (2011, 2013). Direct imaging of the near field of a propagating rupture allows us to compare the laboratory rupture to a kinematic rupture simulation using elastodynamic Green's functions. We compare the case of weak and strong bimaterial contrast and test single-force and double-couple source models to find the source mechanism depending on the elastic contrast and type of slip event.

Experimental setup

All results are derived from the dynamic wave field imaging of two experimental scenarios: sliding of an asperity along an interface with a strong or a weak bimaterial contrast (Fig. 1). The strong bimaterial contrast is constituted of a glass - hydrogel (Polyvinyl-alcohol - PVA) interface (Fig. 1(a)-(b)) and the weak bimaterial contrast by a hydrogel-hydrogel interface (Fig. 1(d)). Since the hydrogels are homemade and non-standardized, an elasticity contrast has to be assumed between them. The frictional behaviour is ensured by a sand patch mimicking an asperity on a smooth surface. The glass plate is moved by a Kollmorgen stepper motor, which induces the deformation then subsequent sliding of the partly blocked gel via the frictional contact of the sand asperity. Seismic radiation is emitted upon failure of frictional contacts due to stick-slip ruptures, and is observed by ultrasonic speckle correlation imaging. The observation plane is centered in the gel, perpendicular to the interface and reaches from the asperity to the gel surface.

The imaging methodology is exemplary shown in Fig. 1(c) with data from the weak interface experiment. Ultrasound backscatter images show a zone of high reflectivity at the gel-gel interface at 4 cm depth. It is caused by the sand layer and the presence of air in between the two hydrogels. Imaging below the interface is feasible, but the speckle quality is deteriorated due to strong ultrasound backscattering. In both gels, a 1 cm thick layer of intermediate reflectivity is observed next to the sand. It is likely caused by increased deposition of the backscatter agent (graphite). While graphite changes the ultrasonic impedance, shear wave propagation at the frequencies of interest remains unaffected. The phase correlation of successive ultrasound speckle images allows to resolve the shear wave induced vertical particle displacement between two snapshots, which is the apparent particle velocity $\frac{\partial u_z}{\partial t}$ (Pinton et al., 2005).

The dynamic observation is made possible by the high velocity contrast of the shear and compression waves in the hydrogel: while the compressional ultrasound travels at approximately $1500\,\mathrm{m\,s^{-1}}$, the rupture induced shear waves propagate at speeds below $10\,\mathrm{m\,s^{-1}}$. Plane ultrasound pulses at high frame rate allow for the shear wave particle velocity to be temporally well resolved ($\Delta_t = 0.33\,\mathrm{ms}$). The ultrasound frequency (5 MHz) ensures the spatial resolution ($\lambda_{US} = 0.3$ mm). Hence, a shear wave propagating at $7\,\mathrm{m\,s^{-1}}$ and 250 Hz is sampled at 25 US-wavelengths per shear wavelength ($\lambda_{shear} = 7$ mm). Consequently, the z-component of the entire transverse displacement field, including near-field terms, is observed.

Kinematic modeling of the radiated wavefield

The observed wavefields radiated by the slip events are compared to direct kinematic wavefield modeling of equivalent body-force models (see section S2.6-S2.8) In each case, we compare the single-force and the douple-couple solutions. The source moves to simulate propagation of rupture fronts, and its velocity as well as the local source time functions are manually adjusted to obtain a good match to the data.

The displacement $u_{ij}(x,t)$ due to a unidirectional force (UF) in the x_j-direction with a source time function $X_0(t)$ at the source position is the convolution of X_0 with the elastodynamic impulse response (Green's function G_{ij}). It is the superposition of the compression and shear wave far-fields and the elastic near-field:

$$\begin{aligned} u_i(\vec{x},t) =& X_0 * G_{ij} \\ =& X_0 * {G_{ij}}^{Near} + X_0 * {G_{ij}}^{Far-P} + X_0 * {G_{ij}}^{Far-S} \end{aligned} \tag{1}$$

The full expression is given in Section S2.6 and a thorough derivation can be found in Aki and Richards (2009) Chapter 3-4.

In contrast to the UF-solution in Eq. (1), the Green's function for a double-couple (DC) model can be separated into five physically meaningful terms: Near-field, intermediate S-field and P-field, and far S-field and P-field.

$$G_{DC} = G^{Near} + G^{IP} + G^{IS} + \quad G^{FP} + G^{FS} \tag{2}$$

The full analytical solution for the displacement field of a DC source can be found in Section S2.7.

In the following, we first present the results on the strong and weak contrast bimaterial interface and then discuss their relevance for natural rupture processes.

Strong bimaterial contrast

The wavefield observations for the strong bimaterial contrast (movie S1) reveals two types of slip events at the asperity: strongly localized micro-slips, and moving rupture fronts that propagate along the asperity and cause a global stick-slip behaviour (see fig S6). We analyze one event of each type, representative of the overall observations.

For the microslip event, depicted in Fig. 2(a), a spherical wavefront is radiated from one location on the asperity. No rupture propagation is observed and consequently we model the

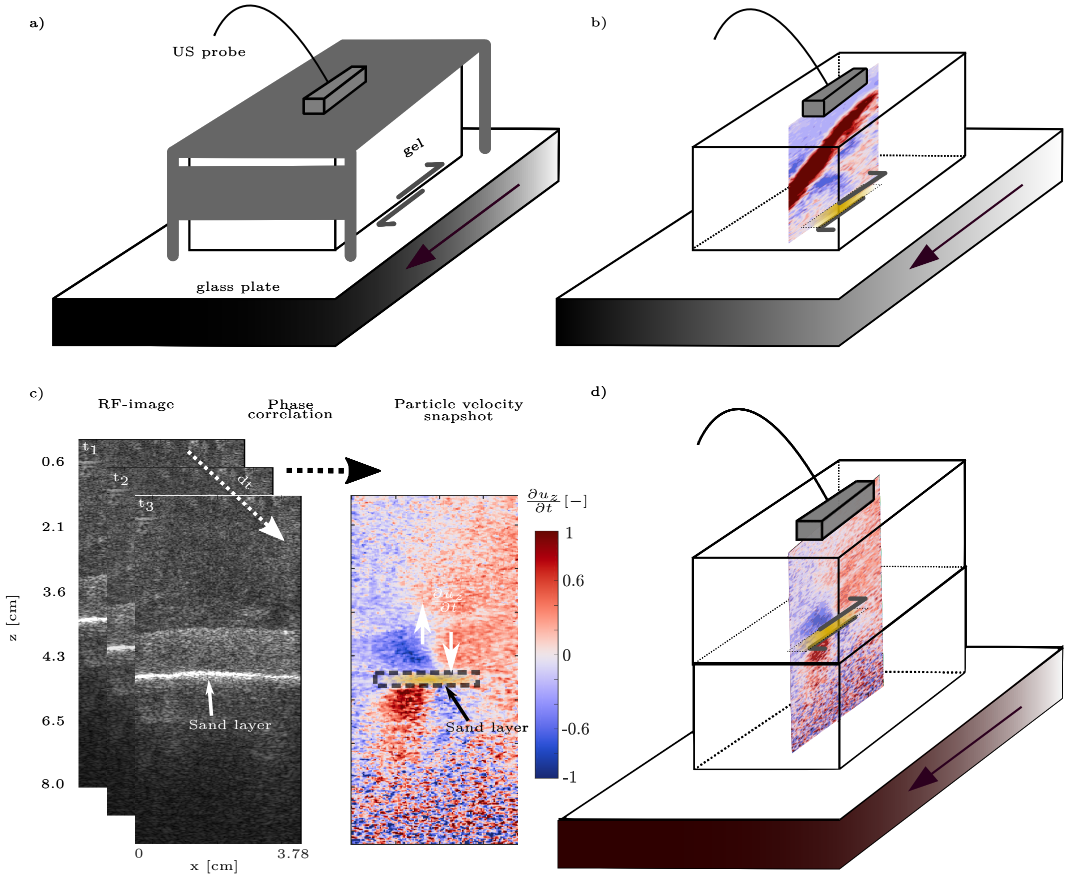

Figure 1. Experimental setup and imaging methodology. (a) Schematic view of the montage. The gel is free at the interface and blocked above. (b) Imaging methodology: Correlation of successive US reflection images results in retrieval of the vertical component of the shear wave's particle velocity. Blue denotes upwards polarization (negative z) and red denotes downwards polarization (positive z). (b) and (d) Schematic illustration of the imaging plane in the bimaterial setups: (b) A hydrogel - sand asperity - glass interface constitutes the strong bimaterial contrast. (d) A hydrogel - sand asperity - hydrogel constitutes the weak bimaterial contrast. A detailed acquisition and processing workflow is given in Fig. S1.

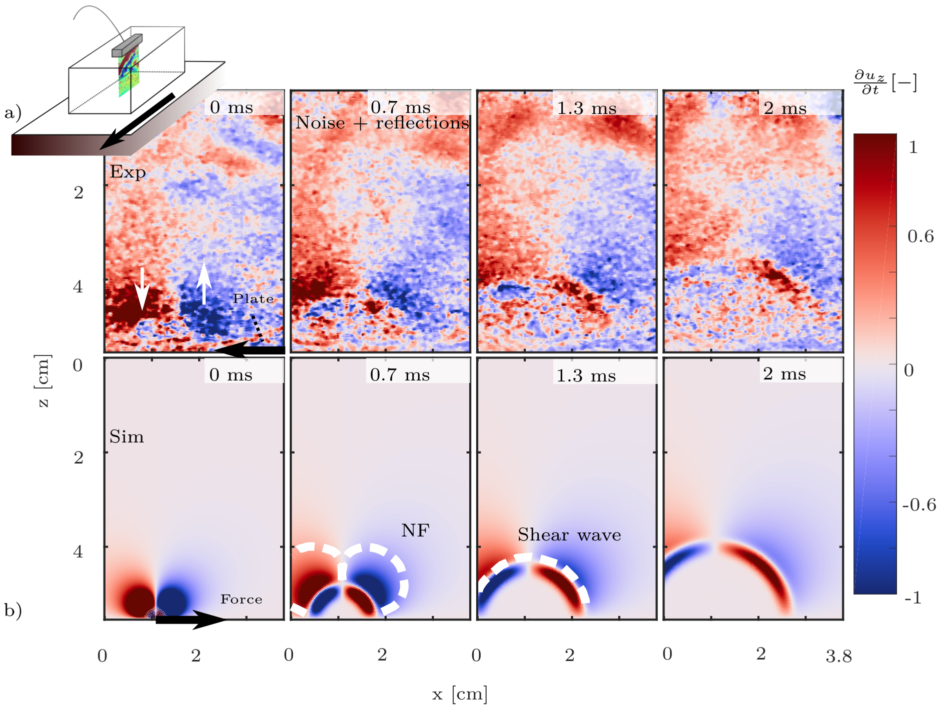

Figure 2. Strong material contrast: Comparison of an experimental micro-slip and simulation. Particle velocity direction is indicated by the white arrows. (a) Particle velocities $\frac{\delta u_z}{\delta t}$ observed by shear wave imaging. The stepper motor drives the plate in negative x-direction. (b) Complete Green's function for displacement u_z of a singular unidirectional shear force in positive x-direction. A median filter was applied to visually highlight the coherent wavefronts. All images are scaled by their extreme values. The near field lobe (NF) and shear wave front are indicated in panels (b).

event with a local point source. The experimental radiation pattern is well reproduced by a unidirectional single force model, as shown in Fig. 2(b) using a ramp shaped source time function $X_0(t)$. The first lobe represents the near field (NF) lobe of the Green's function and is quickly attenuated. The second lobe is of opposite polarity and represents the far-field shear wave. The top 2 cm are artifacts of a previous event (see Fig. S2 event 2-3). In contrast to the simulation, the experiment undergoes constant charging from the motor. Thus, noise as well as aseismic displacement due to deformation are present in the snapshots.

The gaussian source time function of the force employed by Latour et al. (2011) to model depinning events of hydrogel on sand paper fails to reproduce the here observed wavefield. Our ramp shaped source time function with rise time of 0.1ms (see Fig. S10) results in a better match. The plate displacement deforms the gel and a likely physical explanation is a localized change from a high- to low-stress state, which we model by a ramp function in time of a rightward point force (see Fig. S10). Dynamically, this is equivalent a left-pointing loading force applied to the gel, which drops to zero value, corresponding to a shear friction drop localized on a micro-asperity. In the granular layer it might correspond to a highly localized inelastic dislocation or grain micro-slip.

The localized event of Fig. 2 precedes a larger event, in which a rupture front traverses the entire visible interface (see Fig. 3 (a) and Figs. S3-S4 for details). The rupture propagation direction equals the sliding direction of the gel, *i.e.* opposite to the plate movement. This observation agrees with Dedontney et al. (2011), who found that for bimaterial interfaces, ruptures will preferentially propagate in slip direction of the compliant side. The particle velocity ($\frac{\delta u_z}{\delta t}$) measurements in Fig. 3 (a) are compared to two analytic, kinematic simulations: a moving unidirectional force (UF) Fig. 3(b), and a moving double-couple (DC) Fig. 3(c). The simulations result from superposition of point sources along a decelerating speed profile, which is estimated roughly from the experimental data. Through trial and error we qualitatively match the near field lobe, supershear- and rupture arrest front. The source parameters are given in Figs. S10-S14.

Key properties of the unidirectional force model, which are also present in the experimental observation, are indicated in Fig. 3 (b). The first phase is an upwards polarized nonplanar lobe with a diffuse front. It corresponds to the near-field (NF) of the right-traveling and rightwards pointing shear force. A sharp, downwards polarized large amplitude wave front follows, which is identified as a supershear front in the simulation. It is the result of a rupture that breaks the asperity faster than the medium's shear wave speed. The front angle with the x-axis (β=21.8°) at late observation times in Fig. 3 (a) and the measured shear wave speed (c_s) of $6.9\,\mathrm{m\,s^{-1}}$ $\pm 1\,\mathrm{m\,s^{-1}}$ (see Fig. S15) are used to calculate an average rupture propagation speed (c_r) of $\approx 18\,\mathrm{m\,s^{-1}}$: $c_r = \frac{c_s}{sin(\beta)}$. However, two front angles can be identified throughout the rupture (see Fig. S17). Furthermore, a time of flight measurement of the supershear front along the rupture surface (see Fig. S16) suggests a rupture speed above time resolution on 1 cm and below $12\,\mathrm{m\,s^{-1}}$ afterwards, indicating that the rupture is decelerating. This justifies the use of a decreasing rupture velocity in the kinematic model. A low amplitude, downwards polarized wedge is present above the supershear front. It corresponds to the imprint of the compressional (P) wave, which propagates at $\approx 1500\,\mathrm{m\,s^{-1}}$. Finally, a leftwards propagating and upwards polarized wavefront can be observed in the last snapshots of Fig. 3 (a). In the simulations it is identified as the rupture arrest front (RAF), emitted at the asperity border.

In comparison, the best moving DC solution(Fig. 3 (c)) exhibits a high wavefield complexity which is absent in the experiment and in the UF force simulation. Furthermore, the experimental data lack the leading, downwards polarized polarity of the DC simulation. However, at late times (7 ms), we can observe an upwards polarized front following the supershear front, which has a counterpart in the DC solution (Fig. 3 (c)), but is absent in the UF simulation Fig. 3 (b). To conclude, we find that the moving unidirectional force better matches the near field,the supershear front and the rupture arrest front of the experimental data than the double couple model, but does not capture every detail of the wavefield.

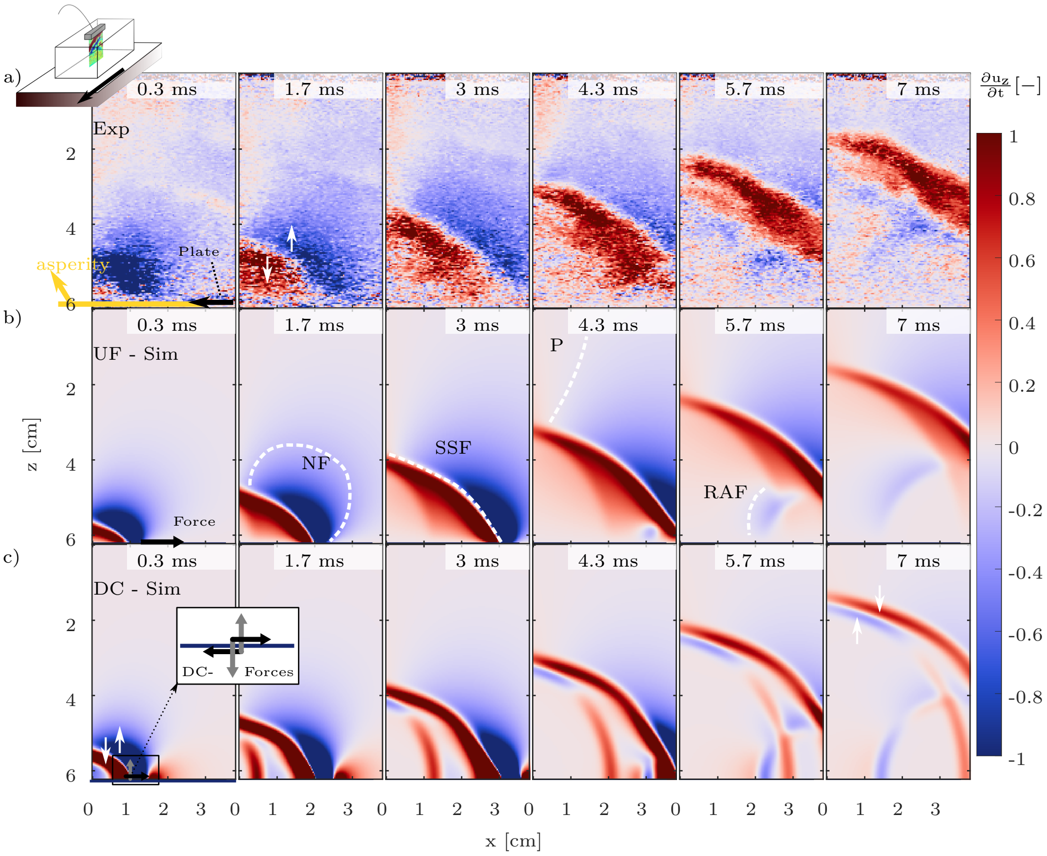

Figure 3. Strong material contrast: Comparison of an experimental supershear rupture and simulation. a) $\frac{\delta u_z}{\delta t}$ as observed by shear wave imaging. The rupture follows the event of Fig. 2. The first snapshot is located 6 ms after the first snapshot of Fig. 2. The motor drives the plate in negative x-direction. b) $\frac{\delta u_z}{\delta t}$ resulting from the superposition of unidirectional shear forces in x-direction. Near field (NF), supershear front (SSF), P-wave imprint (P) and rupture arrest front (RAF) are indicated. c) $\frac{\delta u_z}{\delta t}$ resulting from the superposition of double-couple point sources. The point sources in b) and c) are shifted in time and space, in order to simulate the horizontal advancement of a rupture front (see Supplementary material Section 2.8). All snapshots are normalized with respect to their time-series. The sources are directed in positive x-direction. A higher time-resolution is given in Figs. S4-S5. The source functions and rupture speed profiles can be found in Figs. S11-S12.

Weak bimaterial contrast

We observe again two types of slip events on the weak bimaterial contrast interface: propagating ruptures and localized wave radiations (see movie S2).

A rupture that appears to propagate below shear and Rayleigh wave speed is shown in Fig. 4 (a). Rupture propagation at sub-Rayleigh speed is expected for homogeneous systems (Shlomai & Fineberg, 2016), but has not been observed by shear wave imaging prior to this observation, which is the first dynamic US observation of a gel-gel rupture (Latour et al., 2011). Fig. 4 (c)-(d) show the corresponding 1D waveforms at specified depth- and time-steps in the upper halfspace. In both displays, the right-traveling front exhibits higher amplitudes than the left-traveling one. This front also exposes a smaller angle to the vertical (inclination difference), indicating a speed difference between the fronts. A straightforward explanation is a right-travelling sub-Rayleigh rupture. A wavefront of continuous polarity throughout both half-spaces exists in the rupture propagation direction.

We model the radiation with a double-couple moving to the right at constant sub-Rayleigh velocity (Fig. S13). The simulated wavefield (Fig. 4 (b)-(e)-(f)) reproduces the continuous polarity across the interface. In contrast, the radiation pattern of a unidirectional force exhibits alternating polarities in the two halfspaces (Fig. S9). However, similar to the case of a strong bimaterial contrast, the leading near-field lobe predicted by the double-couple solution is not identified in the experimental data. Fig. 4 a) reveals that a weak upwards polarized zone is present at interface depth, but quickly disappears with depth. This could be an imprint of the near field which gets masked by the continuous deformation of the gel (see movie S2, (Figs. 4 and 5 start at approximately 2396 ms)). Note that the amplitude increase in the rupture direction is reproduced but more pronounced in the simulation than in the experiment. The experiment suffers from shear wave attenuation which is neglected in the kinematic simulation and might mask the amplitude difference between the front in rupture direction and the radiation front in opposite direction. Furthermore, the laboratory rupture might be shorter than the qualitatively simulated rupture of Fig. 4 (b).

Situated three milliseconds after Fig. 4, Fig. 5 (a) shows a localized event with a quadripolar radiation pattern (see Fig. S8 for a comprehensive time-series). The radiation is qualitatively reproduced as the near-field lobe of a unidirectional point force model, which is shown in Fig. 5(b). The source rise time is several ms long (see Fig. S13). Contrary to the localized event on the strong bimaterial contrast interface, the far-field part of the theoretical force radiation is not observed. Instead, the event is followed by a left-going rupture, shown in Fig. 5 (c) (event 3 in Fig. S8). A similar sequence can be observed at 2350 ms in movie S2. One hypothesis is that the long rise-time localized event corresponds to the nucleation process of the subsequent rupture. There appears to be an aseismic lateral displacement of the radiation pattern in the lower half space for the experimental data of unclear origin.

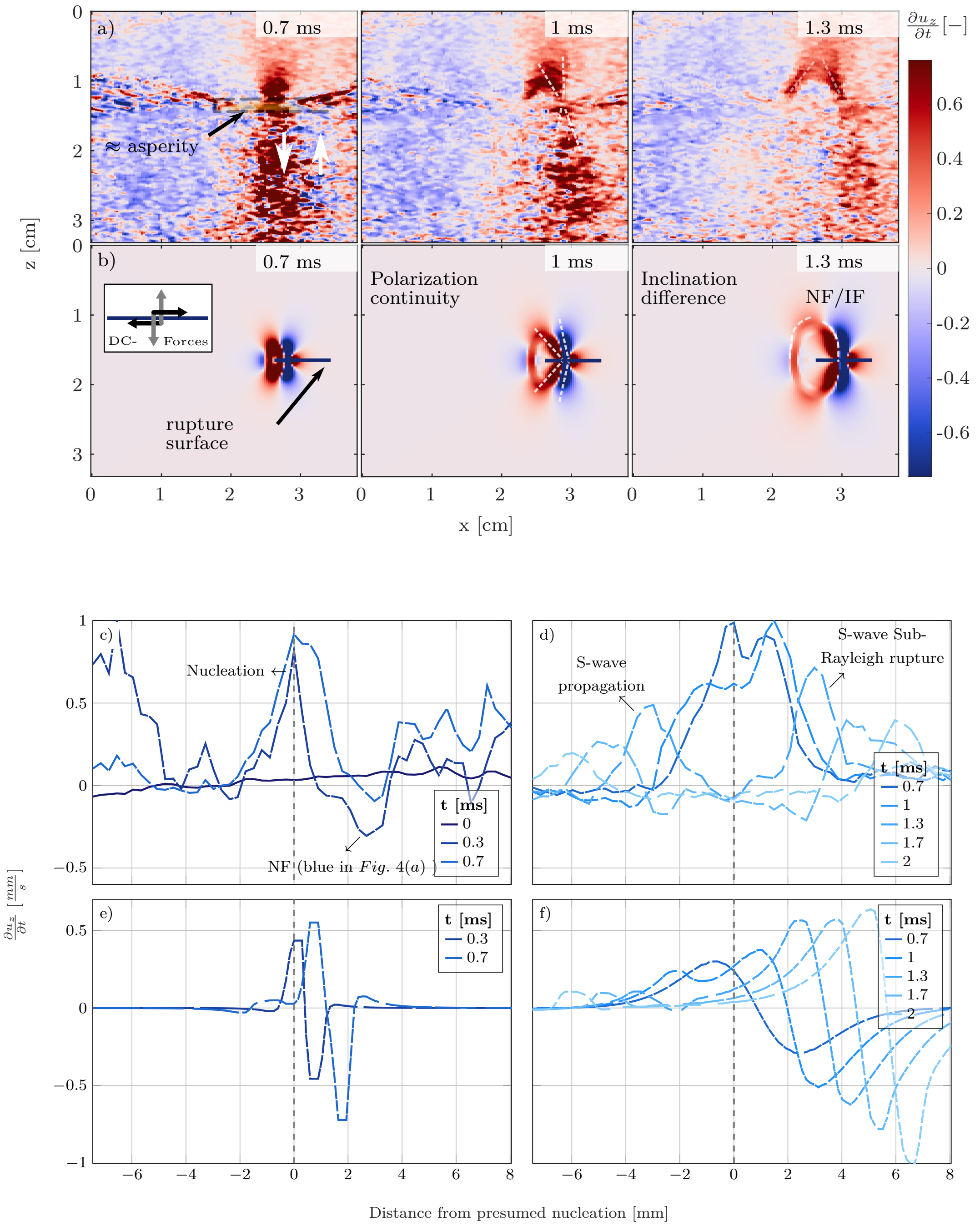

Figure 4. Weak material contrast: Comparison of an experimental sub-Rayleigh rupture and simulation. (a) Experimental particle velocities for a gel-gel rupture. (b) Right-traveling superposition of DC point sources at sub-Rayleigh speed with a ramp source function. The DC-force directions are indicated. The leading near and intermediate fields are indicated as NF/IF. (c)-(f) Spatial Waveforms (x-direction) at fixed depth and time plotted against the distance to the presumed rupture nucleation point. (c) Experimental waveforms during rupture initiation (0 ms - 0.7 ms) at the gel-gel interface. The waveforms are a mean of 27 depthpoints (≈1 mm), just above the sand layer, which was identified from the US reflection images. The relative position of the sand layer to the probe varies about 1.5 mm due to gel deformation and sand thickness. (d) Experimental waveforms of 0.7 to 2 ms ≈ 2 mm above the waveforms in (c). (e) - (f) Simulated waveforms corresponding to (c) and (d). (e) is taken 0.2 mm and (f) 3.8 mm above the simulated interface.

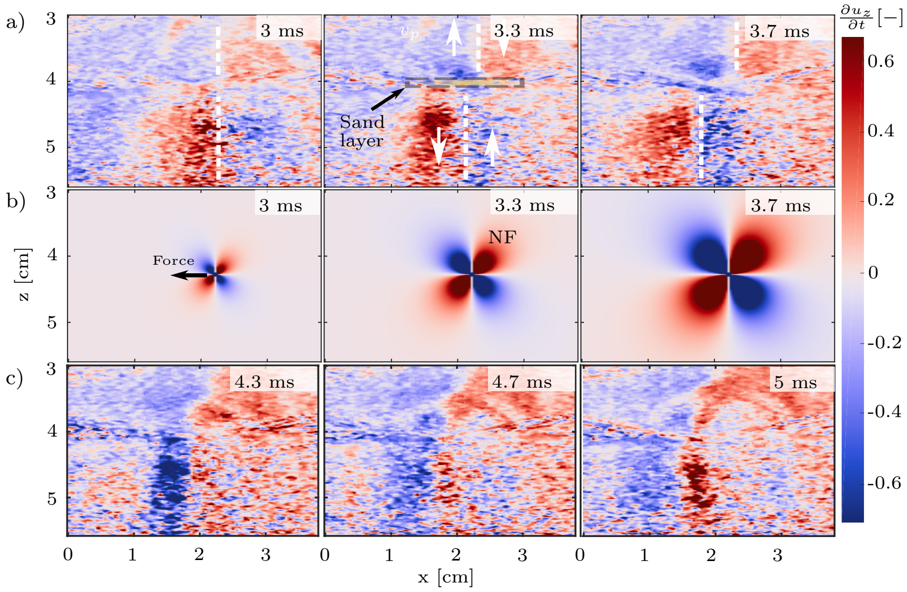

Figure 5. Weak bimaterial contrast: Comparison of an a local event and a UF-simulation. a) The interface is identified by the separation of the upper and lower lobes. Note that imaging quality is deteriorated by US diffraction at the sand, visible in the diagonal artifact in $t = 3$ms and the coarse appearance of the displacement field below the frictional interface. The event happens 3 ms after the rupture shown in Fig. 4. b) Green's function simulation of a localized unidirectional shear force in negative x-direction using a 2.16 ms long rise time for the Gaussian. The near field lobe is indicated as NF. c) Consequent time evolution of (a). The local event is followed or transforms into a rupture (see movie S2 $\approx$ 2400 ms).

Relevance for natural rupture processes

For the strong bimaterial contrast, we find that microslip events as well as propagating ruptures radiations are better described by a unique force model than by a double couple model. This is intuitively understood as due to the strong elastic contrast at the interface: the unidirectional force corresponds to the relaxation of the gel's loading force when friction drops at the interface.

In nature, strong material contrasts are encountered in environmental seismology, i.e. for landslides and glacier stick-slip. Both processes exhibit a wet granular layer and a compliant mass sliding on a hard bedrock. Our granular asperity is conceptually comparable to the "sticky spot" encountered in alpine glacial stick-slip (Umlauft et al., 2021). Unidirectional force source models have been proposed for the 1980 Mt. St. Helens eruption (Kanamori & Given, 1982) and the 1975 Kalapana, Hawaii, earthquake, where a large landslide occurred on Kilauea volcano(Eissler & Kanamori, 1987). In a theoretical analysis Dahlen (1993) showed that a lower shear wave velocity in the brecciated sliding block of shallow landslides results in mechanical decoupling of the two fault sides. The decoupling leads to a single-force rupture source, with the force pointing in the direction of the mass movement for decelerating sliding (Julian et al., 1998). Ekström et al. (2003) found that for glacier stick-slip in Greenland, single force inversions perform better than standard moment tensor inversions. Again, this could be explained by the lower shear wave speed in ice. Lastly, Trottet et al. (2022) very recently showed rupture propagation at supershear speed for snow avalanches, another case exposing low shear wave speeds of the sliding mass ($< 120\,\mathrm{m\,s^{-1}}$). We confirm through direct experimental observation of the wavefield generation that unique force mechanisms are relevant for describing slip events between two materials with strong wave velocity contrasts.

In global seismology, the earthquake source corresponds to slip on a planar fault and is widely modeled by a double couple equivalent body source. Our closest analogue experiment is the case of the propagating rupture on the asperity at the gel-gel interface. We observe radiations best described by a moving double couple , which indicates a symmetry in the strain relaxation process and a coupling between both sides of the fault. However, some ruptures are preceded by localized events which can be described by the near-field radiation of a slowly rising unidirectional force, even though the materials are almost symmetric. We hypothesize that one gel is more deformed than the other during loading. It then begins to relax slowly as a preparatory process before rupture propagation initiation and both gels relax the remaining deformation. This non-symmetric process may be possible thanks to the presence of the sand layer than can locally decouple both sides of the fault through grain rearrangements. The single force source mechanism may be relevant for slow processes on natural faults. Shallow thrust faults for example expose an asymmetry in the fault loading, and fault gouge, damaged layers and fluids can constitute a decoupling mechanism.

Acknowledgements

We are grateful to Christophe Voisin for discussions on rupture nucleation and Max Solazzo for finishing the friction bench. The project has received funding from the European Union's Horizon 2020 research and innovation programme under the Marie Sklodowska-Curie grant agreement No 641943 (ITN WAVES) and resulted in the PHD thesis Aichele (2019). ISterre is part of Labex OSUG@2020.

Open Research section

Data archiving is currently underway and will be archived at: `https://zenodo.org`. Temporary access has been granted via ETH polybox:
`https://polybox.ethz.ch/index.php/s/0r8J638Hs8vlDa0`

References

Aichele, J. (2019). *Elastic waves in complex conditions : From the onset of rupture to viscous dispersion in foams* (Doctoral dissertation, Université de Lyon). Retrieved 2022-01-05, from https://tel.archives-ouvertes.fr/tel-02481746

Aki, K., & Richards, P. G. (2009). Quantitative seismology. In *Book* (Second ed., p. 700). University Science Books. Retrieved from http://books.google.com/books?id=sRhawFG5_EcC&printsec=frontcover%5Cnpapers2://publication/uuid/A2074D09-FE3A-4600-9E91-CA393C8AF127

Ben-Zion, Y., & Ampuero, J.-P. (2009, September). Seismic radiation from regions sustaining material damage. *Geophysical Journal International*, *178*(3), 1351–1356. Retrieved 2022-01-05, from 10/d92gs8 doi: 10/d92gs8

Corbi, F., Funiciello, F., Brizzi, S., Lallemand, S., & Rosenau, M. (2017). Control of asperities size and spacing on seismic behavior of subduction megathrusts. *Geophysical Research Letters*, *44*(16), 8227–8235. doi: 10.1002/2017GL074182

Corbi, F., Funiciello, F., Faccenna, C., Ranalli, G., & Heuret, A. (2011, June). Seismic variability of subduction thrust faults: Insights from laboratory models. *Journal of Geophysical Research*, *116*(B6), B06304. Retrieved from http://doi.wiley.com/10.1029/2010JB007993 doi: 10.1029/2010JB007993

Dahlen, F. A. (1993, February). Single-force representation of shallow landslide sources. *Bulletin of the Seismological Society of America*, *83*(1), 130–143. Retrieved 2022-01-17, from https://doi.org/10.1785/BSSA0830010130 doi: 10/gn47cq

Dedontney, N., Templeton-Barrett, E. L., Rice, J. R., & Dmowska, R. (2011). Influence of plastic deformation on bimaterial fault rupture directivity. *Journal of Geophysical Research: Solid Earth*, *116*(10). doi: 10.1029/2011JB008417

Eissler, H. K., & Kanamori, H. (1987). A single-force model for the 1975 Kalapana, Hawaii, Earthquake. *Journal of Geophysical Research: Solid Earth*, *92*(B6), 4827–4836. Retrieved 2022-07-08, from https://onlinelibrary.wiley.com/doi/abs/10.1029/JB092iB06p04827 doi: 10.1029/JB092iB06p04827

Ekström, G., Nettles, M., & Abers, G. A. (2003, October). Glacial Earthquakes. *Science*. Retrieved 2022-01-05, from 10.1126/science.1088057 doi: 10/cxjwhc

Julian, B. R., Miller, A. D., & Foulger, G. R. (1998). Non-double-couple earthquakes 1. Theory. *Reviews of Geophysics*, *36*(4), 525–549. Retrieved 2022-01-05, from 10/dwdfzv doi: 10/dwdfzv

Kanamori, H., & Given, J. W. (1982). Analysis of long-period seismic waves excited by the May 18, 1980, eruption of Mount St. Helens—A terrestrial monopole? *Journal of Geophysical Research: Solid Earth*, *87*(B7), 5422–5432. Retrieved 2022-07-08, from https://onlinelibrary.wiley.com/doi/abs/10.1029/JB087iB07p05422 doi: 10.1029/JB087iB07p05422

Kavanagh, J. L., Engwell, S. L., & Martin, S. A. (2018, April). A review of laboratory and numerical modelling in volcanology. *Solid Earth*, *9*(2), 531–571. Retrieved 2022-06-15, from https://se.copernicus.org/articles/9/531/2018/ doi: 10.5194/se-9-531-2018

Kwiatek, G., & Ben-Zion, Y. (2013, July). Assessment of P and S wave energy radiated from very small shear-tensile seismic events in a deep South African mine. *Journal of Geophysical Research: Solid Earth*, *118*(7), 3630–3641. Retrieved from http://doi.wiley.com/10.1002/jgrb.50274 doi: 10.1002/jgrb.50274

Kwiatek, G., Plenkers, K., & Dresen, G. (2011). Source parameters of picoseismicity recorded at Mponeng deep gold mine, South Africa: Implications for scaling relations. *Bulletin of the Seismological Society of America*, *101*(6), 2592–2608. doi: 10.1785/0120110094

Latour, S., Gallot, T., Catheline, S., Voisin, C., Renard, F., Larose, E., & Campillo, M. (2011). Ultrafast ultrasonic imaging of dynamic sliding friction in soft solids: The slow slip and the super-shear regimes. *EPL (Europhysics Letters)*, *96*(January 2016), 59003. doi: 10.1209/0295-5075/96/59003

Latour, S., Voisin, C., Renard, F., Larose, E., Catheline, S., & Campillo, M. (2013). Effect of fault heterogeneity on rupture dynamics : An experimental approach using ultrafast ultrasonic imaging. *Journal of Geophysical Research: Solid Earth*, *118*(11), 5888–5902. Retrieved from http://scitation.aip.org/content/asa/journal/jasa/130/4/10.1121/1.3655012 doi: 10.1002/2013JB010231

Lokmer, I., & Bean, C. J. (2010, April). Properties of the near-field term and its effect on polarisation analysis and source locations of long-period (LP) and very-long-period (VLP) seismic events at volcanoes. *Journal of Volcanology and Geothermal Research*, *192*(1-2), 35–47. Retrieved 2022-05-09, from https://linkinghub.elsevier.com/retrieve/pii/S0377027310000521 doi: 10.1016/j.jvolgeores.2010.02.008

Lykotrafitis, G., & Rosakis, A. J. (2006). Dynamic sliding of frictionally held bimaterial interfaces subjected to impact shear loading. *Proceedings of the Royal Society A: Mathematical, Physical and Engineering Sciences*, *462*(2074), 2997–3026. doi: 10.1098/rspa.2006.1703

Pinton, G., Dahl, J., & Trahey, G. (2005, June). Rapid Tracking of Small Displacements with Ultrasound. In *IEEE Ultrasonics Symposium, 2005.* (Vol. 4, pp. 2062–2065). IEEE. Retrieved from http://ieeexplore.ieee.org/document/1603285/ doi: 10.1109/ULTSYM.2005.1603285

Pujol, J. (2003, March). The Body Force Equivalent to an Earthquake: A Tutorial. *SRL*, *74*(2), 163–168. Retrieved from https://pubs.geoscienceworld.org/srl/article/74/4/440/142890 doi: 10.1785/gssrl.74.2.163

Reid, H. (1910). The California Earthquake of April 18, 1906, Report of the State Earthquake Investigation Commission, The Mechanism of the Earthquake. *Nature*, *2*(2128), 165–166. doi: 10.1038/084165a0

Rosakis, A. J., & Coker, D. (1999). Cracks Faster than the Shear Wave Speed. *Science*, *284*(May), 1337–1340.

Rubino, V., Lapusta, N., & Rosakis, A. J. (2022, June). Intermittent lab earthquakes in dynamically weakening fault gouge. *Nature*, 1–8. Retrieved 2022-06-07, from https://www.nature.com/articles/s41586-022-04749-3 doi: 10.1038/s41586-022-04749-3

Rubino, V., Rosakis, A. J., & Lapusta, N. (2020). Spatiotemporal Properties of Sub-Rayleigh and Supershear Ruptures Inferred From Full-Field Dynamic Imaging of Laboratory Experiments. *Journal of Geophysical Research: Solid Earth*, *125*(2), 1–25. doi: 10.1029/2019JB018922

Shlomai, H., & Fineberg, J. (2016). The structure of slip-pulses and supershear ruptures driving slip in bimaterial friction. *nature communications*, *7*, 1–7. Retrieved from http://dx.doi.org/10.1038/ncomms11787 doi: 10.1038/ncomms11787

Trottet, B., Simenhois, R., Bobillier, G., van Herwijnen, A., Jiang, C., & Gaume, J. (2022, January). *Transition from sub-Rayleigh anticrack to supershear crack propagation in snow avalanches.* Retrieved 2022-01-20, from https://www.researchsquare.com/article/rs-963978/v1 doi: 10.21203/rs.3.rs-963978/v1

Umlauft, J., Lindner, F., Roux, P., Mikesell, T. D., Haney, M. M., Korn, M., & Walter, F. T. (2021). Stick-Slip Tremor Beneath an Alpine Glacier. *Geophysical Research Letters*, *48*(2), e2020GL090528. Retrieved 2022-06-17, from https://onlinelibrary.wiley.com/doi/abs/10.1029/2020GL090528 doi: 10.1029/2020GL090528

van Otterloo, J., & Cruden, A. R. (2016, June). Rheology of pig skin gelatine: Defining the elastic domain and its thermal and mechanical properties for geological analogue experiment applications. *Tectonophysics*, *683*, 86–97. Retrieved 2021-12-29, from https://www.sciencedirect.com/science/article/pii/S0040195116302256 doi: 10/f82rbq

2 References from the supplementary material

References

Aki, K., & Richards, P. G. (2009). Quantitative seismology. In *Book* (Second ed., p. 700). University Science Books.

Andrews, D. J., & Ben-Zion, Y. (1997). Wrinkle-like slip pulse on a fault between different materials. *Journal of Geophysical Research: Solid Earth*, *102*(B1), 553–571. doi: 10.1029/96JB02856

Pinton, G., Dahl, J., & Trahey, G. (2005, June). Rapid Tracking of Small Displacements with Ultrasound. In *IEEE Ultrasonics Symposium, 2005.* (Vol. 4, pp. 2062–2065). IEEE. doi: 10.1109/ULTSYM.2005.1603285

Sandrin, L., Catheline, S., Tanter, M., Hennequin, X., & Fink, M. (1999, October). Time-Resolved Pulsed Elastography with Ultrafast Ultrasonic Imaging. *Ultrasonic Imaging*, *21*(4), 259–272. doi: 10.1177/016173469902100402